HIGHER ORDER METHOD OF MOMENTS FOR BISTATIC SCATTERING FROM 2D PEC ROUGH SURFACE WITH GEOMETRIC MODELING BY NURBS SURFACE

A.-Q. Wang[1, *], L.-X. Guo[1], Y.-W. Wei[1], and J. Ma[2]

[1]School of Science, Xidian University, No. 2 Taibai Road, Xi'an, Shaanxi, China

[2]Science and Technology on Space Simulation Laboratory, Beijing, China

Abstract—The higher order method of moments (HMOM) has been proposed to calculate the bistatic scattering from two-dimensional (2D) perfectly electric conducting (PEC) rough surface in this paper. The electric field integral equation (EFIE) is solved through the HMOM with the hierarchical higher order basis functions which are the modified Legendre polynomials. The non-uniform rational B-spline (NURBS) surface is applied to model the plane surface related to the rough surface. Validity of this approach is shown by comparing the bistatic scattering coefficient (BSC) to that of lower order MOM (LMOM) with the Rao-Wilton-Glisson (RWG) or rooftop basis function. This approach has fewer segments in the parametric directions than the LMOM with rooftop basis, and is more efficient for the fewer unknowns and requires less memory than the LMOM with RWG basis. Properties of bistatic scattering from a 2D Gaussian rough surface are also exhibited and analyzed.

1. INTRODUCTION

Electromagnetic (EM) wave scattering from the rough surface has been extensively studied over the past decades and is a popular topic to researchers [1–4], for its important role in surface physics, satellite remote sensing, radar data interpretation and signal processing problems. There have been many methods to solve this scattering problem such as the methods based on the approximate analytical

method and the numerical methods from the Maxwell's equations. Three of the most widely used analytical methods are the Kirchhoff approximation (KA) [5], the small perturbation method (SPM) [5], and the small slope approximation (SSA) [6]. Numerical methods have more general applicability and have been widely presented to compute the EM scattering from rough surface [7–9]. In these numerical methods, the MOM technique [10] is more widespread and accepted for its high accuracy. Unfortunately, the number of unknowns with the 2D rough surface modeled by the flat triangular patch is extremely large, which leads to the computational requirements increasing and impossible to solve by the LMOM with the RWG basis [11] on the personal computer. When there are 64 discrete points both along the x and y directions, the surface current unknowns will be $N = 11781$ with the flat triangular patch. New geometric modeling methods have been considered to reduce the number of unknowns, such as, the quadrilateral patch [12] and the NURBS surface [13]. The number of unknowns will be $N = 8096$ with the quadrilateral patch or $N = 760$ with the NURBS surface to deal with the scattering problem mentioned above. It is obviously found that the number of unknowns with the NURBS surface has been greatly reduced.

A hierarchical higher order basis includes the lower order basis, e.g., the RWG [11] and the rooftop [14]. Here, the modified Legendre polynomials [15], which impose the continuity between neighboring elements and maintain most of their satisfied characters, have been chosen as the hierarchical higher order basis. And this hierarchical higher order basis has lower matrix condition number than the power series [16]. To directly generate the impedance matrix, the position vectors of the source points and field points will be repeatedly computed for different orders and consumed time. In this paper, the position vectors have been independently calculated on the orders of the basis functions to reduce the computing time. When the EFIE is discretized with the hierarchical higher order basis function to a matrix equation, the $1/R$ singularity will be inevitable. In [16], the integral has been divided into two parts on account of Taylor's formula. In [17], the singularity cancelation method has been applied to treat the singular integrals via coordinate transformation. In this study, the singular integrals are treated by dividing the source patch into five sub-patches. The integrand of the four edge sub-patches is handled similar as the nonsingular parts. The singularity subtraction method [18] is applied in the middle sub-patch.
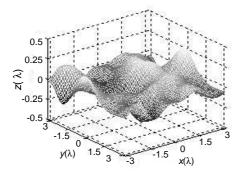
The purpose of this paper is efficiency and accuracy in calculating the bistatic scattering from 2D PEC rough surface by the HMOM based on the previous work [13, 19–22] of our research teams. To

our knowledge, this is the first time that the HMOM is introduced to calculate the BSC of rough surface, and the BSC is obtained and compared to that of LMOM with RWG or rooftop basis function to verify the validity.

This paper is organized as following. There are three points in Section 2: (1) modeling the 2D rough surface with the NURBS surface; (2) definition of the hierarchical higher order basis functions; (3) formulas of bistatic scattering from 2D PEC rough surface calculated through the HMOM method. Section 3 presents the optimized process in generating the impedance matrix and the treatment of the singular integrals. Validity of the technique proposed in this paper is firstly shown in Section 4. Several numerical results and analyses are also exhibited in Section 4 to discuss the influences of polarization, rms height and correlation length of the Gaussian rough surface on the BSC. Section 5 ends with a summary of this paper and the proposition about further investigation in this topic.

2. FORMULAS

2.1. Modeling the 2D Rough Surface with the NURBS Surface

How to simulate a 2D Gaussian rough surface is proposed in detail in [12]. In this study, δ and l are the rms height and the correlation length of the Gaussian rough surface, respectively. The edge length of the Gaussian rough surface is denoted by L. Figure 1 illustrates a geometric model of a 2D Gaussian rough surface, where $\delta = 0.1\lambda$, $l = 1.0\lambda$, $\Delta x = \Delta y = 0.1\lambda$ and $L = 6.3\lambda$. Definition of the NURBS surface is shown in [23].
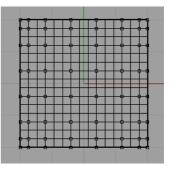

Figure 1. Geometry of a 2D Gaussian rough surface.

Figure 2. A plane surface modeled by the NURBS surface.

To model the Gaussian rough surface with the NURBS surface, the plane surface ($z = 0$) related to the rough surface is firstly modeled by the NURBS surface (see Figure 2). Then the control points, the degrees and the weights for each control points can be obtained through the IGES standard. After obtaining the height function of the Gaussian rough surface, the control points of the plane surface are replaced by the corresponding data of the rough surface. The weights and degrees of the plane surface are still used. Then the Gaussian rough surface can be reconstructed by the parameters of the plane surface and its height function.

2.2. Definition of the Hierarchical Higher Order Basis Functions

Definition of the higher order basis functions for MOM calculations are given in [24] based on the higher order geometry. In this paper, the modified Legendre polynomials proposed by Jørgensen et al. [15] are presented as the hierarchical higher order basis functions as following, which impose the continuity between neighboring elements and maintain most of their satisfied characters.

$$\tilde{p}_m(u) = \begin{cases} 1 - u & m = 0 \\ 1 + u & m = 1 \\ p_m(u) - p_{m-2}(u) & m \geq 2 \end{cases} \tag{1}$$

and $p_m(u)$ is the Legendre polynomial and satisfies

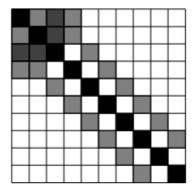$$p_m(u) = \frac{1}{2^m m!} \frac{d^m}{du^m} \left(u^2 - 1 \right)^m \tag{2}$$

Figure 3. The normalized inner product matrix $[\mathbf{S}^{1D}]$ for the modified Legendre polynomial $\tilde{p}_m(u)$.

Then the elements of the normalized inner product matrix $[\mathbf{S}^{1D}]$ can be defined as

$$\mathbf{S}^{1D} = \int_{-1}^{1} \tilde{p}_m(u)\tilde{p}_n(u)du \tag{3}$$

The normalized inner product matrix $[\mathbf{S}^{1D}]$ for the modified Legendre polynomial $\tilde{p}_m(u)$ is illustrated in Figure 3. One can observe that $\tilde{p}_m(u)$ provides a diagonally strong $[\mathbf{S}^{1D}]$.

Using the higher order basis function of the modified Legendre polynomials of (1), the u-directed current $\mathbf{J}_s^u(u, v)$ can be written as

$$\mathbf{J}_s^u(u, v) = \frac{\mathbf{r}_u(u, v)}{|\mathbf{r}_u(u, v) \times \mathbf{r}_v(u, v)|} \times \sum_{n=0}^{N_u - 1} \sum_{m=0}^{N_u} \alpha_{mn} \tilde{C}_m^u \tilde{p}_m(u) C_n^v p_n(v) \tag{4}$$

where, $\tilde{p}_m(u)$ is the modified Legendre polynomial, $p_n(v)$ the Legendre polynomial, and $\mathbf{r}_u(u, v)$ and $\mathbf{r}_v(u, v)$ the u-directed and v-directed partial derivatives, respectively. N_u is the order of $\mathbf{J}_s^u$, and α_{mn} are unknown coefficients. $\tilde{C}_m^u$ and C_n^v are defined as

$$\tilde{C}_m^u = \begin{cases} \frac{\sqrt{6}}{4} & m = 0, 1 \\ \sqrt{\frac{(2m-3)(2m+1)}{4(2m-1)}} & m \geq 2 \end{cases} \tag{5}$$

$$C_n^v = \sqrt{n + \frac{1}{2}} \tag{6}$$

The surface divergence of $\mathbf{J}_s^u(u, v)$ is

$$\nabla_s \cdot \mathbf{J}_s^u(u, v) = \frac{1}{|\mathbf{r}_u(u, v) \times \mathbf{r}_v(u, v)|}$$

$$\times \sum_{n=0}^{N_u - 1} \sum_{m=0}^{N_u} \alpha_{mn} \tilde{C}_m^u \frac{d}{du} \left[\tilde{p}_m(u)\right] C_n^v p_n(v) \tag{7}$$
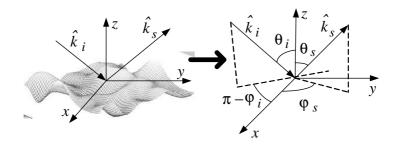
The v-directed current $\mathbf{J}_s^v(u, v)$ and surface divergence $\nabla_s \cdot \mathbf{J}_s^v(u, v)$ are defined similar as those in (4) and (7), respectively.

2.3. Formulas of Bistatic Scattering from 2D PEC Rough Surface by the HMOM

Suppose an EM wave impinging upon a 2D PEC Gaussian rough surface with the height function $z(\mathbf{r}_s)$ as shown in Figure 4. The time dependence is $e^{-i\omega t}$, and the incident wave propagates in the $-z$ direction. $\hat{\mathbf{k}}_i = \hat{\mathbf{x}} \sin\theta_i \cos\varphi_i + \hat{\mathbf{y}} \sin\theta_i \sin\varphi_i - \hat{\mathbf{z}} \cos\theta_i$, where θ_i and φ_i are the incident angle and incident azimuth angle. $\hat{\mathbf{k}}_s = \hat{\mathbf{x}} \sin\theta_s \cos\varphi_s +$

Figure 4. Geometric model of bistatic scattering from a 2D PEC Gaussian rough surface.

$\hat{\mathbf{y}} \sin \theta_s \sin \varphi_s + \hat{\mathbf{z}} \cos \theta_s$, θ_s and φ_s are the scattered angle and the scattered azimuth angle.

To avoid the artificial edge diffraction resulting from the finite length of the simulated rough surface, the incident wave can not be simply chosen as a plane wave, and should be expressed as a Gaussian beam which has a Gaussian shape with half-width W centered at $\mathbf{r}_s = \mathbf{0}$ in the $z = 0$ plane. Consider an incident Gaussian beam, which uses a summation of plane waves, illuminating the geometry model as shown in Figure 4, which is exhibited as [12]

$$\mathbf{E}^{inc}(\mathbf{r}_s) = \frac{2\pi W^2}{L^2} \sum_{|\mathbf{K}| \leq k_0} \hat{\mathbf{e}}^{inc}(\mathbf{K}) \exp(i\mathbf{K} \cdot \mathbf{r}_s)$$

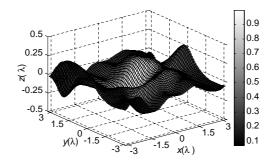$$\times \exp(-ik_z z) \exp \left[-(\mathbf{K} - \mathbf{K}_0)^2 W^2/2 \right] \qquad (8)$$

here, $\mathbf{K}_0 = k_0(\sin\theta_i \cos\varphi_i \hat{\mathbf{x}} + \sin\theta_i \sin\varphi_i \hat{\mathbf{y}})$. L denotes the edge length of the rough surface. The summation over $\mathbf{K} = k_x\hat{\mathbf{x}} + k_y\hat{\mathbf{y}}$ is computed with k_x and k_y being multiples of $2\pi/L$. k_z satisfies $k_z = \sqrt{k_0^2 - (k_x^2 + k_y^2)}$ for each $\mathbf{K}$, and

$$\hat{\mathbf{e}}^{inc}(\mathbf{K}) = \begin{cases} \frac{1}{\sqrt{k_x^2+k_z^2}}(k_z, 0, k_x) & V \\ \frac{(k_x k_y, -(k_x^2+k_z^2), -k_y k_z)}{k_0(k_x^2+k_z^2)^{1/2}} & H \end{cases} \qquad (9)$$

V and H indicates the incident Gaussian beam is considered at vertical or horizontal polarization. The magnitude of the Gaussian beam normally incident on a 2D Gaussian rough surface is shown in Figure 5.

Then the EFIE for solving the surface current unknown $\mathbf{J}(\mathbf{r})$ is [25]

$$\hat{\mathbf{n}} \times \mathbf{E}^{inc}(\mathbf{r}) = \hat{\mathbf{n}} \times -ik_0\eta_0 \times \int_S \left[\mathbf{J}(\mathbf{r}')G(\mathbf{r}, \mathbf{r}') + \frac{1}{k_0^2}\nabla' \cdot \mathbf{J}(\mathbf{r}')\nabla G(\mathbf{r}, \mathbf{r}') \right] dS \quad (10)$$

Figure 5. Magnitude of a Gaussian beam normally incident on a 2D Gaussian rough surface.

$\hat{\mathbf{n}}$ represents the unit normal vector of the rough surface. η_0 is the wave impedance, and $G(\mathbf{r}, \mathbf{r}')$ indicates the Green's function in the free space, i.e.,

$$G(\mathbf{r}, \mathbf{r}') = \frac{\exp(ik_0 R)}{4\pi R} = \frac{\exp(ik_0|\mathbf{r} - \mathbf{r}'|)}{4\pi|\mathbf{r} - \mathbf{r}'|} \qquad (11)$$

To discretize the EFIE, the surface current unknown $\mathbf{J}(\mathbf{r})$ is expanded into a set of hierarchical higher order basis function, and the Galerkin technique is applied as the testing function. Then the EFIE can be converted into the following matrix equation

$$\bar{\bar{\mathbf{Z}}} \cdot \bar{\mathbf{I}} = \bar{\mathbf{V}} \qquad (12)$$

where, $\bar{\bar{\mathbf{Z}}}$ is the impedance matrix with elements [16]

$$Z_{mn} = -ik_0\eta_0 \times \int_{S_m}\int_{S_n}\left[\mathbf{W}_m \cdot \mathbf{J}_n - \frac{\nabla \cdot \mathbf{W}_m \nabla' \cdot \mathbf{J}_n}{k_0^2}\right]G(\mathbf{r}, \mathbf{r}')dS_n dS_m \quad (13)$$

$\mathbf{J}_n$ and $\mathbf{W}_m$ are the basis function and the testing function. S_m and S_n are the patches corresponding to $\mathbf{W}_m$ and $\mathbf{J}_n$. And the matrix $\bar{\bar{\mathbf{Z}}}$ can be also written as

$$\bar{\bar{\mathbf{Z}}} = \begin{bmatrix} \bar{\bar{\mathbf{Z}}}^{HH} & \bar{\bar{\mathbf{Z}}}^{HL} \\ \bar{\bar{\mathbf{Z}}}^{LH} & \bar{\bar{\mathbf{Z}}}^{LL} \end{bmatrix} \qquad (14)$$

where, greater than one order of $\mathbf{W}_m$ and $\mathbf{J}_n$ are used to obtain $\bar{\bar{\mathbf{Z}}}^{HH}$, and zero or one order of them are applied to get $\bar{\bar{\mathbf{Z}}}^{LL}$. Similarly, one can compute $\bar{\bar{\mathbf{Z}}}^{HL}$ and $\bar{\bar{\mathbf{Z}}}^{LH}$. How to generate Z_{mn} will be provided in detail in Section 3.

The voltage vector $\bar{\mathbf{V}}$ has elements as

$$V_m = \int\limits_{S_m} \mathbf{E}^{inc}(\mathbf{r}) \cdot \mathbf{W}_m(\mathbf{r}) dS_m \tag{15}$$

and,

$$\bar{\mathbf{V}} = [\bar{\mathbf{V}}^H \bar{\mathbf{V}}^L]^T \tag{16}$$

here, greater than one order of $\mathbf{W}_m$ is applied to compute $\bar{\mathbf{V}}^H$, and zero or one order of $\mathbf{W}_m$ is used to calculate $\bar{\mathbf{V}}^L$.

After solving the matrix Equation (12), the surface current $\mathbf{J}(\mathbf{r})$ is obtained. In the observational direction with $\hat{\mathbf{k}}_s$, BSC can be defined as [12]

$$\sigma_{ab}(\hat{\mathbf{k}}_s, \hat{\mathbf{k}}_i) = \frac{4\pi R^2 (S_R)_a}{P^{inc}} \quad (a, b = V, H) \tag{17}$$

and,

$$(S_R)_a = \frac{|\mathbf{E}_a^{scat}(\hat{\mathbf{k}}_s)|^2}{2\eta_0 R^2} \tag{18}$$

$$P^{inc} = \frac{L^2}{2\eta_0} \frac{4\pi^2 W^4}{L^4} \sum_{|\mathbf{K}| \leq k_0} \exp\left[-(\mathbf{K} - \mathbf{K}_0)^2 W^2\right] \cdot \cos\theta_{\mathbf{K}} \tag{19}$$

where, $\theta_{\mathbf{K}}$ is the incident angle of each plane wave of the Gaussian beam.

3. GENERATING THE IMPEDANCE MATRIX

3.1. Generating the Impedance Matrix

From (13), it is observed that calculating the double integrals is the kernel of generating the impedance matrix. In this study, the rough surface has been modeled by the NURBS surface. Namely, the elements of $\bar{\bar{\mathbf{Z}}}$ are given by

$$Z_{mn} = -ik_0\eta_0 \times \int_{a_{um}}^{b_{um}} \int_{a_{vm}}^{b_{vm}} \int_{a_{un}}^{b_{un}} \int_{a_{vn}}^{b_{vn}} F(u_m, v_m; u_n, v_n) du_m dv_m du_n dv_n \tag{20}$$

and,

$$
\begin{aligned}
F(u_m, v_m; u_n, v_n) =\ & G\left[\mathbf{r}(u_m, v_m), \mathbf{r}'(u_n, v_n)\right] \\
& \times \begin{bmatrix} \mathbf{W}_m(u_m, v_m) \cdot \mathbf{J}_n(u_n, v_n) \\ -\frac{\nabla \cdot \mathbf{W}_m(u_m, v_m) \nabla' \cdot \mathbf{J}_n(u_n, v_n)}{k_0^2} \end{bmatrix}
\end{aligned} \tag{21}
$$

According to the Gauss-Legendre single-integral integration formula, the element Z_{mn} has the form as

$$Z_{mn} = -ik_0\eta_0 \times \sum_{u_m=1}^{P_{u_m}} \sum_{u_n=1}^{P_{u_n}} \sum_{v_m=1}^{P_{v_m}} \sum_{v_n=1}^{P_{v_n}} G_{wu_m} G_{wv_m} G_{wu_n} G_{wv_n} \tilde{F} \quad (22)$$

where, $P_{u_m} \sim P_{v_n}$ and $G_{wu_m} \sim G_{wv_n}$ are degrees and weights of the corresponding Gauss-Legendre integration formula, respectively. $\tilde{F}$ is obtained from

$$\tilde{F} = G\left[\mathbf{r}(\tilde{u}_m, \tilde{v}_m), \mathbf{r}'(\tilde{u}_n, \tilde{v}_n)\right] \times \begin{bmatrix} \mathbf{W}_m(\tilde{u}_m, \tilde{v}_m) \cdot \mathbf{J}_n(\tilde{u}_n, \tilde{v}_n) \\ -D_m D_n \frac{\nabla \cdot \mathbf{W}_m(\tilde{u}_m, \tilde{v}_m) \nabla' \cdot \mathbf{J}_n(\tilde{u}_n, \tilde{v}_n)}{k_0^2} \end{bmatrix} \quad (23)$$

and, $\tilde{u}_m = G_{nu_m}$, G_{nu_m} is the corresponding knot of the Gauss-Legendre integration formula. $\tilde{v}_m$, $\tilde{u}_n$ and $\tilde{v}_n$ have a similar form as $\tilde{u}_m$. D_m and D_n can be expressed as

$$D_m = \begin{cases} \frac{2}{b_{u_m} - a_{u_m}} & \text{for the } u\text{-directed } \mathbf{W}_m \\ \frac{2}{b_{v_m} - a_{v_m}} & \text{for the } v\text{-directed } \mathbf{W}_m \end{cases} \quad (24)$$

$$D_n = \begin{cases} \frac{2}{b_{u_n} - a_{u_n}} & \text{for the } u\text{-directed } \mathbf{J}_n \\ \frac{2}{b_{v_n} - a_{v_n}} & \text{for the } v\text{-directed } \mathbf{J}_n \end{cases} \quad (25)$$

3.2. Optimized Algorithm in Generating the Impedance Matrix

In (22), the position vectors of the source point $\mathbf{r}'(\tilde{u}_n, \tilde{v}_n)$, filed point $\mathbf{r}(\tilde{u}_m, \tilde{v}_m)$ and Green's function $G(\mathbf{r}, \mathbf{r}')$ have been repeatedly evaluated for different orders of $\mathbf{W}_m$ and $\mathbf{J}_n$. It will be time-consuming to directly calculate Z_{mn}. Analyzing the three variables, it is concluded that they are independent of the orders of $\mathbf{W}_m$ and $\mathbf{J}_n$. This issue motivates several improvements to rapidly generate the impedance matrix. In this investigation, an optimized algorithm has been used by independently calculating the position vectors and the Green's function. This idea has been proposed by Notaros to analyze the scattering of a dielectric scatters [26]. Moreover, this idea can be also applied to rapidly calculate the voltage vector V_m and the scattered filed.

Table 1 exhibits the computing time by directly calculating Z_{mn} and the optimized algorithm, where EM scattering from a plane surface and a sphere has been considered. To create the hierarchical higher order basis function, the maximum order is $N_u = 3$ and $N_v = 3$ for both u-directed and v-directed surface current. There are 4 segments along the u and v direction of the plane surface, 10 segments in the u direction

and 5 segments in the v direction of the sphere. The superiority of the optimized algorithm is obvious in Table 1.

3.3. Treatment of the Singular Integrals

When the source patch S_n and the filed patch S_m correspond to the same patch, the $1/R$ singularity will be inevitable. Many methods have been used to deal with the singularity [16, 17]. In this study, the source patch S_n has been divided into five sub-patches as shown in Figure 6. Hence, for $S_n = S_m$, Equation (13) can be also obtained as

$$Z_{mn} = -ik_0\eta_0 \times \int_{S_m} \left[\int_{S_1} F_1 dS_1 + \int_{S_2} F_2 dS_2 + \int_{S_3} F_3 dS_3 \right.$$
$$\left. + \int_{S_4} F_4 dS_4 + \int_{\Delta S} F_\Delta dS_\Delta \right] dS_m \tag{26}$$

and, expressions of $F_1 \sim F_\Delta$ are similar as those in (21).

The integrand of the four edge sub-patches $S_1 \sim S_4$ can be treated similar to the non-singular case of (20). It is necessary to note that $\tilde{u}_n$ and $\tilde{v}_n$ is different from those in (23), and has the following form

$$\tilde{u}_n = \frac{2u_s - (b_{u_n} + a_{u_n})}{b_{u_n} - a_{u_n}} \tag{27}$$

Table 1. The computing time by directly calculating Z_{mn} and the optimized algorithm, respectively.

Model	Directly t_1 (Second)	Optimized t_2 (Second)	t_1/t_2
Plane surface	935.33	36.53	25.6
Sphere	5184.08	331.25	15.65

Figure 6. Dividing the source patch S_n into five sub-patches.

where,

$$u_s = \frac{b_{u_s} - a_{u_s}}{2} G_{nu_s} + \frac{b_{u_s} + a_{u_s}}{2} \tag{28}$$

$\tilde{v}_n$ can be obtained in the same way as that in (27).

The singularity subtraction method, which has been applied in [18] for higher order polynomial vector basis functions on planar triangles, is applied to calculate the integrand of the middle sub-patch ΔS. The Green's function (11) can be decomposed into two parts

$$G(\mathbf{r}, \mathbf{r}') = \frac{\exp(ik_0 R) - 1}{4\pi R} + \frac{1}{4\pi R} \tag{29}$$

And the exponent can be also evaluated in the Taylor's formula

$$\exp(ik_0 R) = 1 + ik_0 R + \frac{(ik_0 R)^2}{2!} + \frac{(ik_0 R)^3}{3!} + \dots \tag{30}$$

Therefore, the first term of (29) can be computed by the Gauss-Legendre integration formula. The right term can be analytically calculated like

$$\int_S \mathbf{f}(\mathbf{r}')dS' = 7.087\sqrt{S}\mathbf{f}_{avg} \tag{31}$$

S indicates the integral area, and

$$\mathbf{f}_{avg} = \mathbf{f}(\mathbf{r}_c) \tag{32}$$

where, $\mathbf{r}_c$ is the centre of S.

4. NUMERICAL RESULTS AND ANALYSES

To ensure validity of the proposed technique in this paper, the angular distribution of the BSC from a 2D PEC Gaussian rough surface has been calculated in Figure 7 by the HMOM, the LMOM with RWG basis and the LMOM with rooftop basis. Both H and V polarized incident waves are considered. Parameters of the incident Gaussian beam are set at $\theta_i = 20°$, $\varphi_i = 0°$ and $W = L/4$ [12]. The edge length of the Gaussian rough surface is $L = 6.3\lambda$, and there are 64 discrete points along both x and y directions. The Gaussian rough surface is modeled by the NURBS surface with 23 control points in each direction of u and v [13]. The rms height and correlation length of the Gaussian rough surface are set to be $\delta = 0.1\lambda$ and $l = 1.0\lambda$.

In performing the LMOM with rooftop basis, the Gaussian rough surface is divided into 20 segments in each parametric direction of u and v. The number of unknowns is $N = 760$ [13]. In this study, only 12 segments are divided in u and v directions. One can obtain that the discrete interval is 0.3λ of the LMOM with rooftop basis

and 0.5λ for the HMOM. In other words, there are fewer segments in the parametric directions of the HMOM than those of the LMOM with the rooftop basis. The HMOM is more efficient in calculating the bistatic scattering from 2D rough surface with large size than the LMOM with the rooftop basis. The maximum order of the hierarchical higher order basis functions is $N_u = 3$ and $N_v = 3$ for the u-directed and v-directed surface current. The number of unknowns will be $N = 2520$ for the HMOM. To solve this scattering problem, the surface current unknowns will be $N = 11781$ of the LMOM with RWG basis. It is obviously concluded that the HMOM is more efficient for fewer unknowns and requires less memory than the LMOM with RWG basis. It is also obvious that, for the LMOM with RWG basis, $N = 11781$ is extremely large and hardly to solve through the conventional MOM [10] on the personal computer. Here, the parallel MOM algorithm with two processors is utilized for the calculation with the RWG basis. As can be seen in Figure 7, the scattering pattern of the HMOM is in good agreement with that of the LMOM with RWG or rooftop basis near the specular direction.

The comparisons of the simulating time and memory requirements by the HMOM, the LMOM with rooftop or RWG basis for the same surface realization is also listed in Table 2, where H and V indicate the polarizations of the incident wave, respectively. The numerical simulations are realized on the computer with a 2.33 GHz processor (Intel Core 2 Quad Q8200), 8 GB Memory, ASUSTekP5Mainboard, Microsoft Windows Server 2003 Enterprise edition and the Visual Fortran 6.5 compiler. MPICH 2.103 has been used. It needs to point out that the simulating time by LMOM with the RWG basis
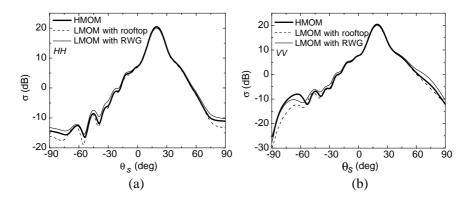

Figure 7. Comparisons of the BSC from a 2D Gaussian rough surface by different methods. (a) HH; (b) VV.

Table 2. The simulating time and the memory requirements of different methods for one same surface realization.

Polarization	Method	Number of unknowns	Memory requirements (MB)	Simulating time (Second)
H	HMOM	2520	98.75	2591.00
	LMOM with rooftop basis	760	10.29	2950.58
	LMOM with RWG basis	11781 (parallel MOM with two processors)	2140.03 (parallel MOM with two processors)	1833.31 (parallel MOM with two processors)
		– (conventional MOM)	– (conventional MOM)	– (conventional MOM)
V	HMOM	2520	98.75	2589.48
	LMOM with rooftop basis	760	10.29	2957.59
	LMOM with RWG basis	11781 (parallel MOM with two processors)	2140.03 (parallel MOM with two processors)	1820.44 (parallel MOM with two processors)
		– (conventional MOM)	– (conventional MOM)	– (conventional MOM)

corresponds to that of parallel MOM with two processors, and it is difficult to give the calculating time by the conventional MOM for the large number of unknowns.

From Table 2, it is readily found that the HMOM spends less time to solve this scattering problem than the LMOM with rooftop basis. Although the HMOM technique saves only a small percentage in terms of simulating time and requires more memory than the LMOM with rooftop basis, there are fewer segments in the parametric directions of the HMOM than those of the LMOM with the rooftop basis. The HMOM is more efficient in calculating the bistatic scattering from

2D rough surface with large size than the LMOM with the rooftop basis. Comparisons of the HMOM and LMOM with RWG basis show that the HMOM can extremely reduce the number of unknowns and memory requirements for both H and V polarizations. The HMOM is more efficient for fewer unknowns and requires less memory than the LMOM with RWG basis. However, calculating the bistatic scattering from a 2D Gaussian rough surface through the HMOM is still time-consuming. The parallel algorithm [13, 27] or the adaptive integral method (AIM) [28] will be introduced in the future work.

    In the next simulations, the properties of bistatic scattering from a 2D PEC Gaussian rough surface are investigated and discussed.
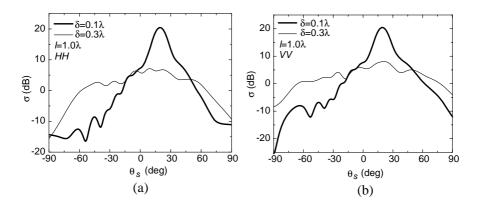

Figure 8. Comparison of the BSC with different rms height: co-polarization. (a) HH; (b) VV.
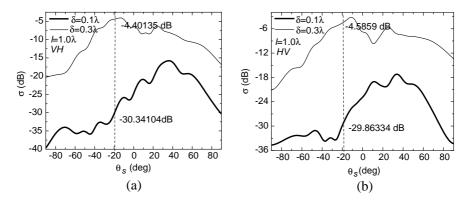

Figure 9. Comparison of the BSC with different rms height: cross-polarization. (a) VH; (b) HV.

The BSC of Gaussian rough surface with different rms heights and correlation lengths for both co-polarization and cross-polarization are illustrated in Figure 8–Figure 11. The Gaussian rough surfaces are all discreted with interval $\Delta x = \Delta y = 0.1\lambda$ and have 64 discrete points along x and y directions. There are 12 segments along both u and v directions. To perform hierarchical higher order basis, the maximum order is still $N_u = 3$ and $N_v = 3$. Parameters of the incident Gaussian beam are $W = L/4$, $\theta_i = 20°$ and $\varphi_i = 0°$. All the numerical results of the BSC are computed by averaging 10 surface realizations.

Figure 8 and Figure 9 show the influences of the rms height δ on the BSC of co-polarization and cross-polarization with the correlation length $l = 1.0\lambda$. For the co-polarization (see Figure 8), there is an obvious peak in the specular direction for the smaller rms height $\delta = 0.1\lambda$ at both HH and VV cases, because the specular peak of the coherent wave strongly depends on the surface roughness, and the roughness of the Gaussian rough surface relies on rms height, smaller rms height, more smoothness of the Gaussian rough surface, leading to the obvious peak in the specular direction. Oppositely, for larger rms height, the Gaussian rough surface becomes rougher and will generate more contribution to the incoherent wave in the non-specular direction. Considering the cross-polarization (see Figure 9), this phenomenon is more obvious because the BSC of the cross-polarization relies more on incoherent wave. With increasing rms height, more energy is scattered by the incoherent wave. Consequently, the incoherent scattering is enhanced with increasing surface roughness. In Figure 9, the backscattering angle is labeled in the dashed line, and the backscattering coefficients are shown. From Figure 9, it is found that the backscattering coefficients satisfy approximately $VH = HV$ at the backscattering angle.

Further investigation on the relationship between the BSC and the correlation length l for both co-polarization and cross-polarization are plotted in Figure 10 and Figure 11, respectively, where the rms height is $\delta = 0.1\lambda$. As apparent in Figure 10, there is a wider band of the BSC near the specular direction for the larger correlation length $l = 1.0\lambda$, and this behavior shows the fact that the height of Gaussian rough surface changes gently for the larger correlation length, which causes a more coherent scattering contribution to the BSC near the specular direction. Whereas, the smaller the correlation length is, the greater the BSC is far from the specular direction for both HH and VV polarizations. The primary reason for this is that by keeping the rms height constant and decreasing the correlation length, the electromagnetic roughness is constant, but the rms slope increases, leading to a higher angular spreading of the scattered energy,

which implies an increase of the scattered energy in the incoherent scattering direction. Similar result is obtained by considering the cross-polarization in Figure 11, but the BSC is greater over the whole scattering regions (including the secular direction) for the small correlation length. Similar to the computing case in Figure 9, from Figure 11, it is also seen that the backscattering coefficients approximately satisfy $VH = HV$ at the backscattering angle.

The azimuth variation of the BSC from the 2D Gaussian rough surface is depicted in Figure 12 for both co- and cross-polarizations, where parameters of the Gaussian rough surface are $\delta = 0.1\lambda$, $l = 0.5\lambda$. The scattered angle is $\theta_s = \theta_i = 20°$. From Figure 12(a), it is readily seen that the BSC has a greatest value with $\varphi_s = 0°$ for both HH and VV polarizations. We attribute this behavior to the fact that the BSC in this azimuth is mainly contributed to the coherent wave. Based on the analysis mentioned above, including the influences of the BSC on the rms height and the correlation length, more coherent scattering contribution to the BSC under this condition ($\delta = 0.1\lambda$, $l = 0.5\lambda$). Oppositely, the BSC is the smallest in this azimuth for the cross-polarization in Figure 12(b). The BSC shows a 'dip' near the azimuth $\varphi_s = 90°$ in Figure 12(a). Namely, the coherent contribution to the BSC is the least in the direction perpendicular to the incident plane, which is built by $\hat{\mathbf{k}}_i$ and $\hat{\mathbf{z}}$. As can be also observed for the co-polarization, the BSC of the VV polarization is greater than that of the HH case for $\varphi_s > 90°$, and for the cross-polarization the BSC of VH polarization is almost the same as that of HV case over the whole scattering azimuth.
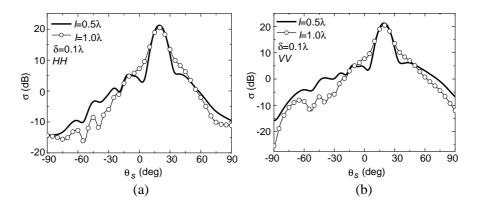

Figure 10. Comparison of the BSC with different correlation length: co-polarization. (a) HH; (b) VV.
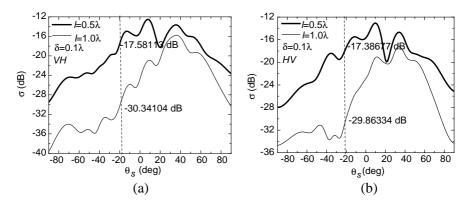
Figure 11. Comparison of the BSC with different correlation length: cross- polarization. (a) VH; (b) HV.
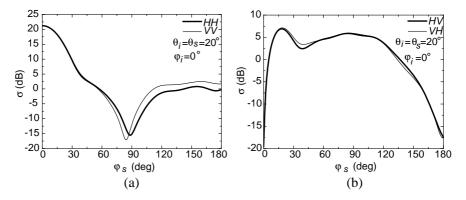

Figure 12. Comparison of the BSC with different scattered azimuth angle. (a) Co-polarization, (b) cross-polarization.

5. CONCLUSION

This paper proposes the HMOM to investigate on the properties of the bistatic scattering from a 2D PEC Gaussian rough surface. The EFIE has been converted to a matrix equation with the hierarchical higher order basis functions and Galerkin technique. And the modified Legendre polynomials have been chosen as the basis function. An optimized algorithm has been applied to rapidly generate the impedance matrix. And a special treatment of the singular integral has also been provided in this study. The validity of this new technique is exhibited by comparing to the LMOM with RWG or rooftop basis.

Compared to the LMOM with rooftop basis, the HMOM has fewer segments in the parametric directions and has fewer unknowns than the LMOM with RWG basis. It is necessary to note that the focus of this study is only on the bistatic scattering from a 2D PEC rough surface. The influences of the backscattering cross section on the incident angle will be discussed in the future. Moreover, it is still time-consuming in calculating the bistatic scattering from a 2D Gaussian rough surface through the HMOM. The parallel algorithm [13, 27] or the AIM technique [28] will be introduced in calculating the scattering from 2D rough surface, especially for the 2D surface with large size in the future work.

ACKNOWLEDGMENT

REFERENCES

1. Xu, P., L. Tsang, and K. S. Chen, "Fourth stokes parameter in polarimetric passive remote sensing from two-layer rough surfaces," *Progress In Electromagnetics Research*, Vol. 129, 125–141, 2012.

2. Zhu, X., Z. Zhao, W. Yang, Y. Zhang, Z. Nie, and Q. H. Liu, "Iterative time-resersal mirror method for imaging the buried object beneath rough ground surface," *Progress In Electromagnetics Research*, Vol. 117, 19–33, 2011.

3. Xu, P. and K. S. Chen, "Analysis of microwave emission of exponentially correlated rough soil surfaces from 1.4 GHz to 36.5 GHz," *Progress In Electromagnetics Research*, Vol. 108, 205–219, 2010.

4. Yang, W., Z. Q. Zhao, C. H. Qi, W. Liu, and Z. P. Nie, "Iterative hybrid method for electromagnetic scattering from a 3-D object above a 2-D random dielectric rough surface," *Progress In Electromagnetics Research*, Vol. 117, 435–448, 2011.

5. Kong, J. A., *Electromagnetic Wave Theory,* John Wiley & Sons, New York, 1986.

6. Voronovich, A. G. and V. U. Zavorotny, "Theoretical model for scattering of radar signals in Ku- and C-bands from a rough sea surface with breaking waves," *Waves in Random Media*, Vol. 11, No. 3, 247–269, 2001.

7. Tsang, L., J. A. Kong, K. H. Ding, et al., *Scattering of Electromagnetic Waves: Numerical Simulations,* John Wiley & Sons, New York, 2001.

8. Li, J., L. X. Guo, and H. Zeng, "FDTD method investigation on the polarimetric scattering from 2-D rough surface," *Progress In Electromagnetics Research*, Vol. 101, 173–188, 2010.

9. Liu, P. and Y. Q. Jin, "Numerical simulation of the doppler spectrum of a flying target above dynamic oceanic surface by using the FEM-DDM method," *IEEE Trans. Antennas Propag.*, Vol. 53, No. 2, 825–832, 2005.

10. Harrington, R. F., *Filed Computation by Moment Method,* IEEE Press, New York, 1993.

11. Rao, S. M., D. R. Wilton, and A. W. Glisson, "Electromagnetic scattering by surfaces of arbitrary shape," *IEEE Trans. Antennas Propag.*, Vol. 30, No. 3, 409–418, 1982.

12. Wagner, R. L., J. M. Song, and W. C. Chew, "Monte carlo simulation of electromagnetic scattering from two-dimensional random rough surfaces," *IEEE Trans. Antennas Propag.*, Vol. 45, No. 2, 235–245, 1997.

13. Wang, A. Q., L. X. Guo, and C. Chai, "Numerical simulations of electromagnetic scattering from 2D rough surface: Geometric modeling by NURBS surface," *Journal of Electromagnetic Waves and Applications*, Vol. 24, No. 10, 1315–1328, 2010.

14. Cátedra, M. F., F. Rivas, and L. Valle, "A moment method approach using frequency independent parametric meshes," *IEEE Trans. Antennas Propag.*, Vol. 45, No. 10, 1567–1568, 1997.

15. Jørgensen, E., J. L. Volakis, P. Meincke, et al., "Higher order hierarchical legendre basis functions for electromagnetic modeling," *IEEE Trans. Antennas Propag.*, Vol. 52, No. 11, 2985–2995, 2004.

16. Yuan, H. B., N. Wang, and C. H. Liang, "Combining the higher order method of moments with geometric modeling by NURBS surfaces," *IEEE Trans. Antennas Propag.*, Vol. 57, No. 11, 3558–3563, 2009.

17. Ding, W. and G. F. Wang, "Treatment of singular integrals on generalized curvilinear parametric quadrilaterals in higher order method of moments," *IEEE Antennas Wireless Propag. Lett.*,

Vol. 8, 1310–1313, 2009.

18. Jarvenpaa, S., M. Taskinen, and P. Y. Oijala, "Singularity subtraction technique for high-order polynomial vector basis functions on planar triangles," *IEEE Trans. Antennas Propag.*, Vol. 54, No. 1, 42–49, 2006.

19. Guo, L. X., A. Q. Wang, and J. Ma, "Study on EM scattering from 2-D target above 1-D large scale rough surface with low grazing incidence by parallel MOM based on PC clusters," *Progress In Electromagnetics Research*, Vol. 89, 149–166, 2009.

20. Wang, R. and L. X. Guo, "Numerical simulations of wave scattering from two-layered rough surface," *Progress In Electromagnetics Research B*, Vol. 10, 63–175, 2008.

21. Guo, L. X., Y. Liang, J. Li, and Z. S. Wu, "A high order integral SPM for the conducting rough surface scattering with the tapered wave incidence TE CASE," *Progress In Electromagnetics Research*, Vol. 114, 333–352, 2011.

22. Li, J., B. Wei, Q. He, L. Guo, and D. Ge, "Time-domain iterative physical optics method for analysis of EM scattering from the target half buried in rough surface: PEC case," *Progress In Electromagnetics Research*, Vol. 121, 391–408, 2011.

23. Zhao, Y., X. W. Shi, and L. Xu, "Modeling with NURBS surfaces used for the calculation of RCS," *Progress In Electromagnetics Research*, Vol. 78, 49–59, 2008.

24. Eastwood, J. W. and J. G. Morgan, "Higher-order basis functions for MoM calculations," *IET Sci. Meas. Technol.*, Vol. 2, No. 6, 379–386, 2008.

25. Song, J. M. and W. C. Chew, "Moment method solutions using parametric geometry," *Journal of Electromagnetic Waves and Applications*, Vol. 9, Nos. 1–2, 71–83, 1995.

26. Notaros, B. M. and B. D. Popovic, "Optimized entire-domain moment-method analysis of 3D dielectric scatterers," *Int J. Numerical Modelling: Electronic Networks, Devices, and Fields*, Vol. 10, 177–192, 1997.

27. Zhang, Y., R. A. Geijn, M. C. Taylor, et al., "Parallel MOM using higher-order basis functions and PLAPACK in-core and out-of-core solvers for challenging EM simulations," *IEEE Antennas and Propagation Magazine*, Vol. 51, No. 5, 42–60, 2009.

28. Lai, B., H. B. Yuan, and C. H. Liang, "Analysis of nurbs surfaces modeled geometries with higher-order MoM based aim," *Journal of Electromagnetic Waves and Applications*, Vol. 25, Nos. 5–6, 683–691, 2012.